nature communications

Article

https://doi.org/10.1038/s41467-026-69612-9

Surface hydroxyl-induced Pt^0 clusters on TiO_2 for synergistic water gas shift catalysis

Received: 19 June 2025

Accepted: 4 February 2026

Published online: 14 February 2026

Check for updates

Cong-Xiao Wang[1], Wei-Wei Wang[1] ✉, Xin-Pu Fu[1], Hao-Xin Liu[2], Feng Ryan Wang[2] & Chun-Jiang Jia[1] ✉

The regulation of active site electronic structure is a central strategy for optimizing supported metal catalysts, yet achieving precise and comprehensive control remains challenging due to the complex nature of metal-support interactions. This work presents a practical and reproducible approach to this challenge through the deliberate regulation of surface hydroxyls on TiO_2 via a titanate-derived synthesis and controlled calcination, which correlates with improved water gas shift catalysis activity of Pt/TiO_2 catalyst. The mechanistic interpretation by multiple characterizations suggest that a higher hydroxyl concentration is associated with the formation of more reduced Pt species, which enhanced CO activation. Subsequently, hydroxyl groups can be directly consumed by CO, which shows a correlation with the formation of oxygen vacancies. Catalysts with a higher density of oxygen vacancies exhibit stronger H_2O dissociation capability. This work develops hydroxyl-content control as a viable strategy for catalyst optimization, supported by a mechanistic framework that rationalizes its impact on both metal electronic structure and oxide surface chemistry.

The water gas shift (WGS) reaction is an important industrial process for hydrogen production and carbon monoxide elimination, where the efficient activation of reactant molecules on the active sites of the catalyst surface is the key determinant of catalytic performance[1]. Supported metal-oxide catalysts have garnered attention due to their high dispersion and stability of metals. On reducible oxide supports, active metal–oxygen vacancies synergy is one possible mechanistic motif for WGS reaction[2,3]. Pt/TiO_2 stands as an exemplary catalytic system that has been extensively investigated in a variety of pivotal reactions, including the WGS reaction, CO oxidation, hydrogenation, and hydrocarbon reforming[4–7]. Currently, due to the electronic metal-support interaction (EMSI) between Pt and TiO_2, electrons at the interface tend to transfer from Pt species to TiO_2, resulting in the formation of $Pt^{\delta+}$-O_v-Ti^{3+} interfacial sites[8–11]. Although such interfacial sites possess unsaturated Ti^{3+} and oxygen vacancies that facilitate the H_2O dissociation[12–14], which frequently is the rate-determining step of the WGS reaction[15,16], the oxidized $Pt^{\delta+}$ species exhibit limited ability for CO activation. This limitation hinders effective matching with the enhanced H_2O dissociation capability, thus restricting the WGS reaction performance. Generally, the enrichment of electron density on Pt sites facilitates the adsorption of CO molecules[2,17]. Therefore, the targeted construction of metallic Pt sites to match the abundant defect structure on the TiO_2 surface represents an effective strategy for further enhancing the WGS reaction, which has been almost overlooked.

Commonly, the electronic structure of metal species is intrinsically linked to their size. The aggregation of metallic Pt particles is often accompanied by the decrease in the dispersion, which, due to geometric effects, results in the loss of active sites[18]. Conversely, ultrasmall species (<1 nm) typically exhibit positively charged metal sites, which lead to weakened CO adsorption[19]. Therefore, precise regulation of the electronic structure of Pt sites while controlling the size of metal species is essential yet challenging. It has been reported that the structure of the active metals is closely related to the surface properties of oxide support, which can be modulated by introducing the

[1]Key Laboratory for Colloid and Interface Chemistry, Key Laboratory of Special Aggregated Materials, School of Chemistry and Chemical Engineering, Shandong University, Jinan 250100, China. [2]Department of Chemical Engineering, University College London, Roberts Building, Torrington Place, London WC1E 7JE, UK. ✉e-mail: wangww@sdu.edu.cn; jiacj@sdu.edu.cn

functional groups onto the support[11,20]. Surface hydroxyl groups have been well established for their roles in regulating catalyst structure, influencing the adsorption of reactant molecules, and participating in reactions[21–23]. Recent research has reached a consensus on the use of surface hydroxyl groups constructed on TiO_2 as direct anchoring sites for active metals, which contributes to maintaining the size of the active metals[24–27]. Moreover, a perspective that surface hydroxyl groups on TiO_2 facilitate hydrogen spillover from metal sites to the support surface has been clearly proposed[28,29]. During the H* transfer process, electrons are retained at the metal sites[30,31]. Consequently, it can be expected to the correlation between the construction of surface hydroxyl groups on TiO_2 support and the enhancement of electron density at Pt sites. Furthermore, the hydroxyl groups, serving as the crucial intermediates in the WGS reaction[7,32], are capable of directly reacting with CO adsorbed on Pt^0 sites. This consumption is anticipated to generate the high density of defect sites throughout the catalytic process, thereby facilitating the activation and dissociation of more H_2O molecules. However, the effectiveness of hydroxyl groups does not always exhibit the positive correlation with their abundance. This is attributed not only to the blocking of metal sites by excess hydroxyl groups, but also to the fact that there exists an optimal amount of hydroxyl groups for modulating the state of the active species[33,34]. Therefore, precise modulation of the hydroxyl content is essential for achieving optimal catalytic performance[35,36].

In this work, we developed a practical and reproducible hydroxyl-regulation approach via controlled calcination of a titanate precursor to tailor the structure of Pt/TiO_2 catalysts. This method enabled the formation of small Pt^0 clusters (~2 nm) on the hydroxyl-tuned TiO_2 surface, distinct from conventional common $Pt^{\delta+}$-O_v-Ti^{3+} interfacial structure. Multiple characterization indicated that the resulting Pt species was consistent with the more reductive electronic state, which enhanced CO adsorption and activation. Furthermore, hydroxyl groups were consumed under CO exposure, a process that correlated with the generation of oxygen vacancies. Catalysts with a higher density of oxygen vacancies exhibited stronger H_2O dissociation capability. A reasonable mechanistic interpretation was that the synergistic combination of the strong CO adsorption on Pt^0 and efficient H_2O dissociation enabled the excellent reaction rate of 62.7 $mol_{CO}{\cdot}g_{Pt}^{-1}{\cdot}h^{-1}$ and the turnover frequency (TOF) of 6.15 s^{-1} at 250 °C in WGS reaction, which were nearly 2–3 times greater than the Pt/TiO_2 catalysts in the literature. This work thus offered a practical handle for tuning catalytic activity via hydroxyl regulation, alongside insights into how such tuning modulated the metal electronic and oxide surface structure.

Results

Regulation of hydroxyl content for the formation of target Pt/TiO_2 catalysts

The scheme of regulating the hydroxyl content on the support to obtain the target Pt/TiO_2 catalyst is shown in Fig. 1a. Commercial anatase (denoted as TiO_2-A) was hydrothermally treated with the highly concentrated NaOH solution (10 mol/L), followed by washing with HCl solution. This process resulted in the phase transformation from anatase to $H_2Ti_3O_7$, which was denoted as TiO_2-T-UC (Supplementary Fig. S1). It was imperative to elucidate the surface structure of the modified TiO_2 and the chemical state of the supported Pt species. Firstly, according to the O 1*s* XPS spectra compared to that of TiO_2-A, the peak of lattice oxygen in TiO_2-T-UC shifted toward the higher binding energy, which originated from the distinct layered titanate structure of the $H_2Ti_3O_7$ phase compared to the anatase phase (Fig. 1b)[37]. Moreover, the another peak at 531.4 eV was attributed to bridging hydroxyls and the weak peak appearing at 532.6 eV was considered to be adsorbed hydroxyl groups from the environment, which originated from the absence of any thermal treatment[38]. The results of ATR-IR and TGA experiments also confirmed the formation of abundant surface hydroxyls (Supplementary Fig. S2). However, the nanotubular morphology of TiO_2-T-UC caused the supported Pt species to be completely embedded in the TiO_2 support lattice during the WGS reaction (Supplementary Fig. S3). The observed hindrance of CO molecule adsorption and the suppression of activity also confirmed this encapsulation (Supplementary Fig. S4, S5 and Table S1). Therefore, further thermal treatment of TiO_2-T-UC in the air atmosphere was conducted (Supplementary Fig. S6). As the calcination temperature increased, the nanotubular morphology of TiO_2 progressively collapsed, leading to the exposure of previously encapsulated Pt species (Supplementary Fig. S7 and S8). Concurrently, the hydroxyl concentration decreased with rising calcination temperature, resulting in the increase in the size of the supported Pt species (Supplementary Fig. S9 and S10). By integrating the hydroxyl group content with the exposure and size of Pt species, the Pt-based catalyst supported on TiO_2-T calcined at 500 °C (denoted as TiO_2-T-500) exhibited the optimal catalytic activity (Fig. 1c). It was worth noting that O 1*s* XPS spectra of TiO_2-T-500 showed that adsorbed hydroxyl groups disappeared due to thermal treatment, but the residual bridging hydroxyls were still present (Fig. 1b). Moreover, the mass loss from hydroxyls desorption of TiO_2-T-500 in the TGA experiments was 1.19 %, while that of TiO_2-A was only 0.20 % (Fig. 1d), demonstrating that the TiO_2-T-500 support possessed the higher abundance of surface hydroxyl groups compared to TiO_2-A (Fig. 1e)[35]. The H − D exchange and ATR-IR experiment also indicated the hydroxyl groups on TiO_2-T-500 were more abundant than those on TiO_2-A (Supplementary Fig. S11). These results revealed that TiO_2-T-500 support with optimal hydroxyls content was obtained through the two-step hydroxylation-thermal treatment process of TiO_2-A.

As reported, the surface properties of the support are closely related to the state of the supported active metals. The aberration-corrected HAADF-STEM characterization revealed that in the fresh 0.3Pt/(TiO_2-T-500) catalyst, Pt species primarily coexisted as single atoms and clusters, which was consistent with the state of Pt species in the fresh 0.3Pt/(TiO_2-A) catalyst (Fig. 1f, g). After the WGS reaction, the aggregation of Pt species into clusters occurred in both catalysts (Fig. 1h–k and Supplementary Fig. S12 and S13). Statistical analysis of Pt species indicated that the average size in the spent 0.3Pt/(TiO_2-T-500) catalyst was 1.6 nm, which was quite similar to the 1.7 nm observed in the spent 0.3Pt/(TiO_2-A) catalyst (Supplementary Fig. S14). Moreover, CO chemisorption measurements revealed that the dispersions of the spent 0.3Pt/(TiO_2-T-500) and 0.3Pt/(TiO_2-A) catalysts were 55.2% and 48.1%, respectively (Supplementary Table S1). The non-identical dispersions were derived from CO uptake based on a 1:1 CO:Pt stoichiometry, which might be influenced by various factors, such as support-dependent spillover, dynamic readsorption, or differences in CO binding strength. Nevertheless, they served as a supplementary indication that the Pt clusters in both catalysts remained accessible after reaction. This assessment was consistent with the direct HAADF-STEM observation of similar mean particle sizes after reaction. However, the predominant Pt^0 species were present in the spent 0.3Pt/(TiO_2-T-500) catalyst, while the $Pt^{\delta+}$ species were predominant in the spent 0.3Pt/(TiO_2-A) catalyst (Supplementary Fig. S4). This observation suggested that the hydroxyl groups constructed on the support induced the significant changes in the electronic structure of Pt species in the absence of size effects.

The formation of Pt^0 species induced by hydroxyls for enhanced CO activation

To thoroughly investigate the influence of hydroxyls on the electronic structure of active metals, the H_2 pretreatment process prior to the reaction was taken into consideration, which might induce changes in the catalyst structure. Having ruled out the influence of H_2 reduction temperature on hydroxyl groups and H_2O desorption (Supplementary Fig. S15a, b), the temperature-programmed reduction by H_2 (H_2-TPR,

https://doi.org/10.1038/s41467-026-69612-9

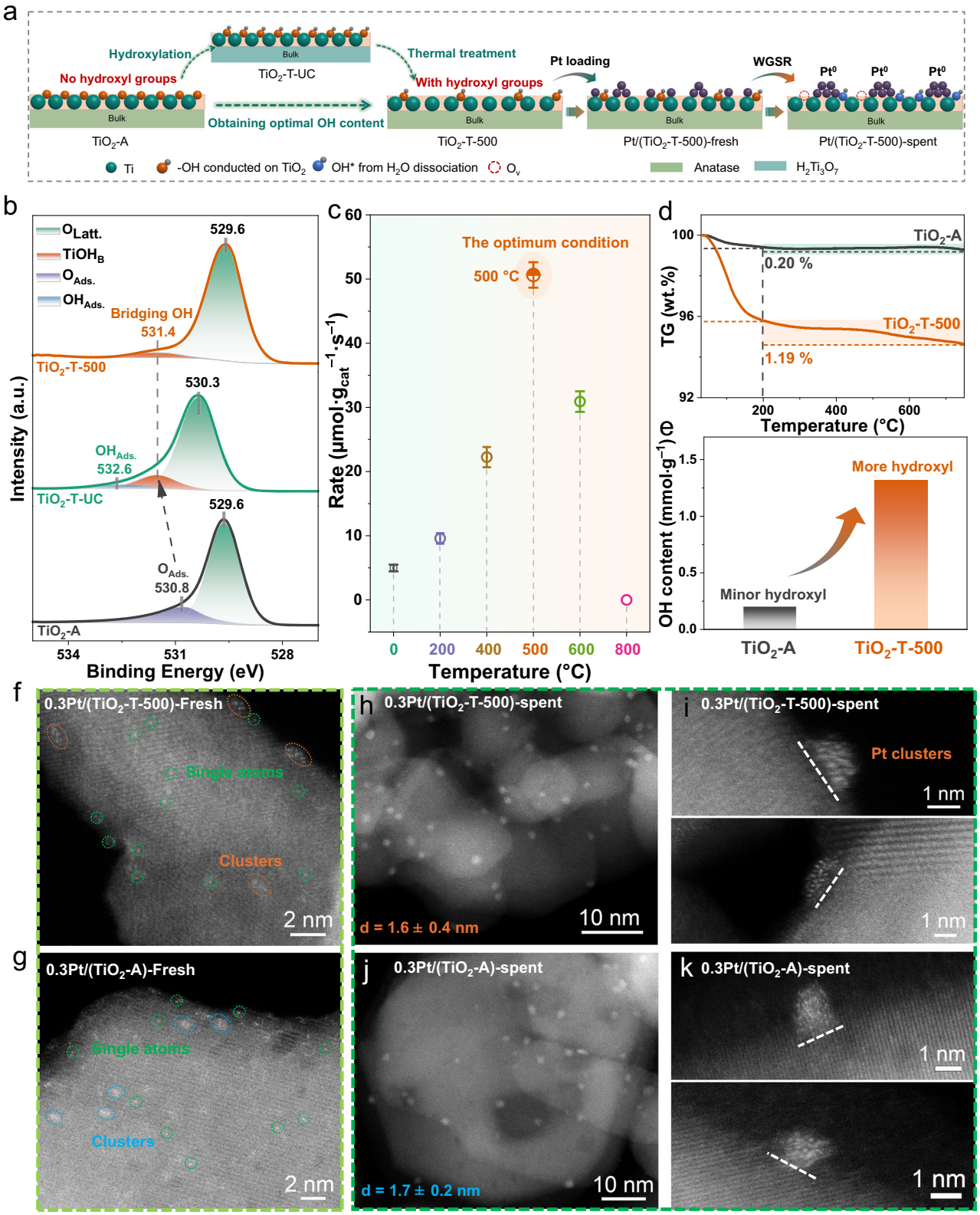

Fig. 1 | Construction of Pt/TiO_2 catalysts with the optimal hydroxyls content on the support. a Scheme of regulating the hydroxyl content on the support to obtain the target Pt/TiO_2 catalyst. **b** O 1*s* XPS spectra of TiO_2-A, TiO_2-T-UC and TiO_2-T-500 supports. **c** WGS reaction rate of Pt/TiO_2 catalyst at 250 °C as the function of calcination temperature of TiO_2-T support, with the optimum at 500 °C. Reaction condition: 2% CO/10% H_2O/N_2. The error bars are defined as standard deviation, and the center of each error bar represents the mean value of three independent experiments. **d** TGA curves of TiO_2-A and TiO_2-T-500 supports. **e** The hydroxyl content of TiO_2-A and TiO_2-T-500 supports determined from TGA measurements. Aberration-corrected HAADF-STEM images of the fresh (**f**) 0.3Pt/(TiO_2-T-500) and (**g**) 0.3Pt/(TiO_2-A) catalyst. Aberration-corrected HAADF-STEM images of the spent (**h**, **i**) 0.3Pt/(TiO_2-T-500) and (**j**, **k**) 0.3Pt/(TiO_2-A) catalyst.

https://doi.org/10.1038/s41467-026-69612-9

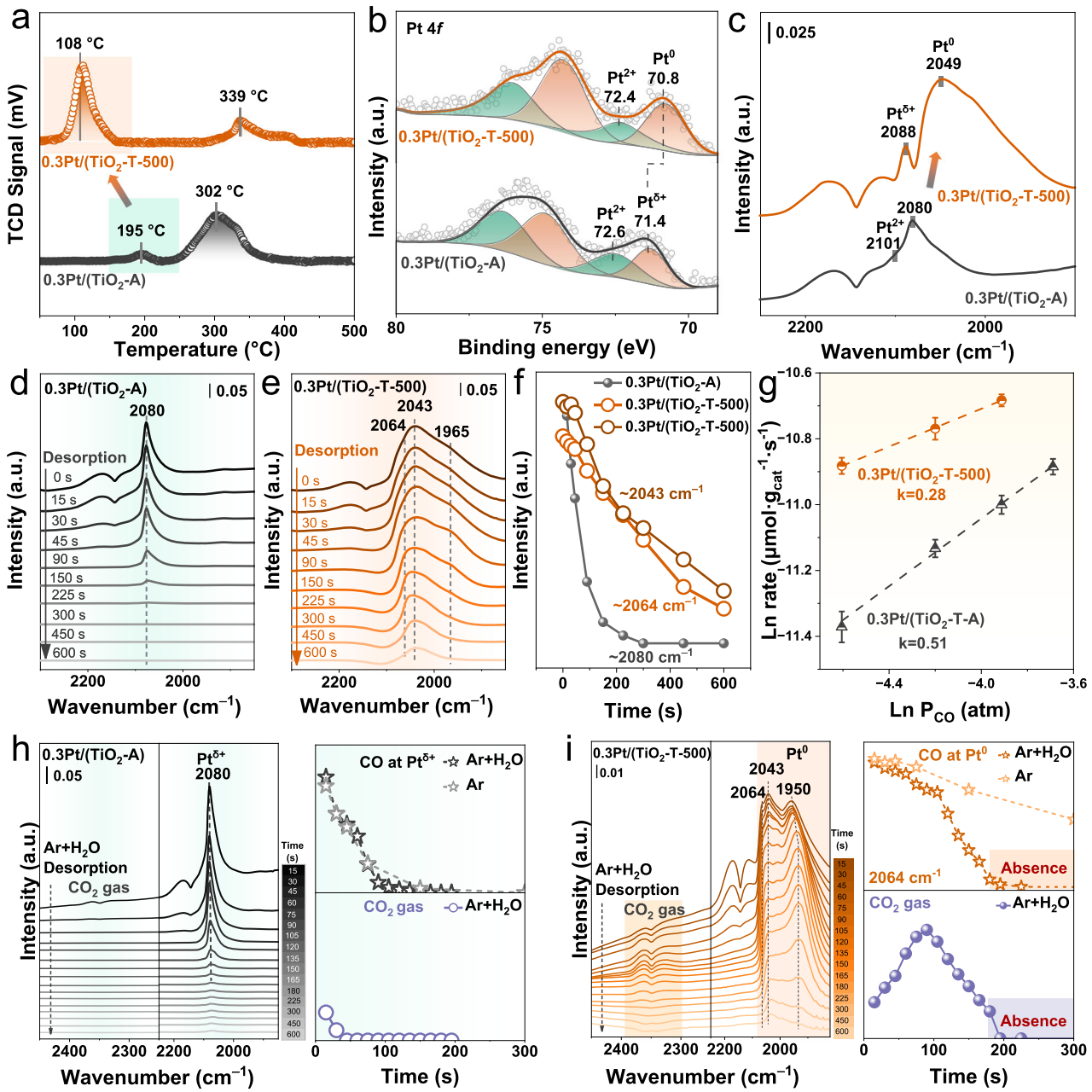

Fig. 2 | Surface hydroxyl-induced Pt^0 for enhanced CO activation. a H_2-TPR profiles of 0.3Pt/(TiO_2-T-500) and 0.3Pt/(TiO_2-A) samples. **b** Ex situ Pt 4*f* XPS for 0.3Pt/(TiO_2-T-500) and 0.3Pt/(TiO_2-A) samples after H_2 pretreatment. **c** In situ DRIFTS spectra of the CO adsorption for 0.3Pt/(TiO_2-T-500) and 0.3Pt/(TiO_2-A) samples after H_2 pretreatment. In situ DRIFTS spectra after WGS reaction of Ar purging over (**d**) 0.3Pt/(TiO_2-A) and (**e**) 0.3Pt/(TiO_2-T-500) at 250 °C. **f** The intensity of CO adsorption bands with the function of time for (**d**, **e**). **g** Kinetic orders of CO at 250 °C of 0.3Pt/(TiO_2-A) and 0.3Pt/(TiO_2-T-500) catalyst. The error bars are defined as standard deviation, and the center of each error bar represents the mean value of three independent experiments. In situ DRIFTS spectra of Ar+H_2O purging over (**h**) 0.3Pt/(TiO_2-A) and (**i**) 0.3Pt/(TiO_2-T-500) at 250 °C. Right: the intensity of CO adsorption on Pt sites upon Ar+H_2O and Ar purging as function of time.

Fig. 2a) showed that the significant decrease in the reduction temperature of the 0.3Pt/(TiO_2-T-500) catalyst compared to 0.3Pt/(TiO_2-A). This elucidated that the construction of surface hydroxyls on the TiO_2-T-500 support was beneficial to the reduction of catalyst, which was further evidenced by the higher hydrogen consumption observed in 0.3Pt/(TiO_2-T-500) catalyst (Supplementary Fig. S15c). According to the Pt 4*f* XPS spectra, the Pt species in the fresh 0.3Pt/(TiO_2-T-500) and 0.3Pt/(TiO_2-A) catalysts exhibited Pt^{2+} species at 72.5 eV and 72.3 eV, respectively (Supplementary Fig. S16)[39,40]. After H_2 pretreatment, the Pt in the 0.3Pt/(TiO_2-A) catalyst showed the binding energy of 71.4 eV, corresponding to $Pt^{\delta+}$ (Fig. 2b)[41,42]. In contrast, the binding energy for the 0.3Pt/(TiO_2-T-500) catalyst shifted down by 0.7 eV to 70.8 eV, which likely correlated with the presence of Pt^0[43]. This result was consistent with the superior reducibility of the 0.3Pt/(TiO_2-T-500) catalyst compared to 0.3Pt/(TiO_2-A), facilitating the reduction of Pt^{2+} to Pt^0 during H_2 treatment. Furthermore, the XANES profile at Pt L_3 edge spectra revealed the lower white-line intensity for 0.3Pt/(TiO_2-T-500) compared to 0.3Pt/(TiO_2-A) (Supplementary Fig. S17), which indicated that the Pt species in 0.3Pt/(TiO_2-T-500) possessed the higher 5 d electron density, corresponding to the more Pt^0 sites[44]. However, considering the poor signal-to-noise ratio and interference from H* adsorption under H_2 atmosphere, this result could not fully

represent the exact state of Pt species under the WGS reaction, which could only imply a stronger tendency for Pt species in 0.3Pt/(TiO_2-T-500) to be in the metallic state compared to that in 0.3Pt/(TiO_2-A). Moreover, in situ DRIFTS experiments with CO adsorption showed that the weak reducibility of 0.3Pt/(TiO_2-A) catalyst resulted in the presence of Pt^{2+} and $Pt^{\delta+}$ ($0<\delta<2$) species, observed at 2101 cm^{-1} and 2080 cm^{-1}, respectively[45,46]. In contrast, while the Pt^{2+} species disappeared in the 0.3Pt/(TiO_2-T-500) catalyst, a new band appeared at 2049 cm^{-1}. Its red shift relative to the $Pt^{\delta+}$ band in 0.3Pt/(TiO_2-A) was associated with its assignment to Pt^0 species, consistent with literature and electronic effects[46–50]. While we acknowledge that band positions can also be influenced by factors such as particle size and CO coverage, the observed trend across the sample series, combined with the supporting HAADF-STEM images, XPS and XANES data, leads us to attribute the dominant effect to the modification of the Pt electronic state. Overall, the observed trends were consistent with a mechanistic interpretation wherein support hydroxylation promoted the formation of Pt species with the more metallic electronic character.

During the subsequent WGS reaction, the active metal typically served as the adsorption and activation site for the reactant molecule CO. In situ DRIFTS experiments revealed the Pt^0 species in 0.3Pt/(TiO_2-T-500) and the $Pt^{\delta+}$ species in 0.3Pt/(TiO_2-A) formed during the H_2 pretreatment, which remained under WGS reaction condition (Supplementary Fig. S18). To explore the adsorption capability of CO molecules on Pt species with different electronic states in the two catalysts, Ar atmosphere was switched from WGS reaction atmosphere in the in situ DRIFTS experiment (Fig. 2d, e). The $Pt^{\delta+}$ species in 0.3Pt/(TiO_2-A) catalyst showed limited affinity for CO adsorption, with nearly complete desorption occurring within 3 minutes under Ar gas (Fig. 2d). For 0.3Pt/(TiO_2-T-500) catalyst, in addition to the bridged CO signal at 1950 cm^{-1} originating from the metal-support interface, CO linear adsorption on the masked Pt^0 sites at 2064 cm^{-1} emerged during Ar purging, which were closer to the interfacial sites compared to the Pt^0 at 2043 cm^{-1} (Fig. 2e)[47,49]. Notably, the interfacial signal at 2064 cm^{-1} remained red-shifted compared to the $Pt^{\delta+}$ signal at 2080 cm^{-1} in 0.3Pt/(TiO_2-A), indicating that the interfacial Pt sites in the 0.3Pt/(TiO_2-T-500) catalyst possessed higher electron density, consistent with the state of Pt^0 clusters. The persistence of CO adsorption strength for the two kinds of Pt^0 species in the 0.3Pt/(TiO_2-T-500) catalyst after 10 min of Ar gas purging indicated that the Pt^0 induced by surface hydroxyls exhibited the stronger CO adsorption capability (Fig. 2f). Moreover, the enhanced binding of CO on the 0.3Pt/(TiO_2-T-500) catalyst was further evidenced by the CO desorption temperature in the CO-TPD experiment (Supplementary Fig. S19), which was 30 °C for 0.3Pt/(TiO_2-A) and significantly lower than the 65 °C observed for 0.3Pt/(TiO_2-T-500). Furthermore, the kinetic orders of CO for the 0.3Pt/(TiO_2-T-500) catalyst was 0.07 at 220 °C and 0.27 at 250 °C, which was one-third of the value for the 0.3Pt/(TiO_2-A) catalyst at 220 °C and half of their value at 250 °C (Fig. 2g and Supplementary Fig. S20). The decrease in the CO reaction order further provided evidence for the significantly enhanced adsorption capability of CO molecules by Pt^0 species in the 0.3Pt/(TiO_2-T-500) catalyst.

It has been reported that the electronic structure of Pt species in the WGS reaction has been a subject of considerable controversy[45,51]. To accurately elucidate the activation capability of CO by Pt species with different electronic structures, in situ DRIFTS experiments were employed at 250 °C, involving switching between CO and Ar or Ar+H_2O for adsorption and desorption steps. For the 0.3Pt/(TiO_2-A) catalyst, after eliminating interference from surface oxygen on the gaseous CO_2 signal (Supplementary Fig. S21), Ar and Ar+H_2O atmosphere was switched from CO adsorption (Fig. 2h and Supplementary Fig. S22). The CO adsorbed on the oxidized $Pt^{\delta+}$ species of 0.3Pt/(TiO_2-A) catalyst showed similar desorption rates under both Ar+H_2O and Ar atmospheres and the concurrent decrease in the gaseous CO_2 signal, which indicated that $Pt^{\delta+}$ species was not the efficient catalytic site. In contrast, the CO adsorbed on both the Pt^0 species in the 0.3Pt/(TiO_2-T-500) catalyst at 2064 cm^{-1} and at 2043 cm^{-1} exhibited the significantly accelerated consumption rate under Ar+H_2O purging compared to Ar purging, accompanied by the gaseous CO_2 signal that initially increased and subsequently decreased (Fig. 2i and Supplementary Fig. S23). This indicated that CO adsorbed on Pt^0 sites reacted with H_2O and generated additional CO_2. As the adsorbed CO on Pt^0 was progressively consumed, the production of CO_2 gradually diminished and eventually vanished upon complete purging. These results collectively pointed to the superior ability of Pt^0 in activating CO molecules. In addition, the CO on the Pt^0 species near the interface at 2064 cm^{-1} was completely consumed after 200 s, and correspondingly, CO_2 was no longer generated. Meanwhile, the CO signal on the Pt^0 away from the interface at 2043 cm^{-1} remained present, but continued injection of H_2O could not generate additional CO_2 (Supplementary Fig. S24). These results revealed that the Pt^0 closer to the interface was more active in activating CO molecules. It was noteworthy that in bimolecular redox reactions, instantaneous dynamic changes in the oxidation state of active sites at the interface were ubiquitous. DFT calculations and Bader charge analysis revealed the charge on the Pt_1 atom in the Pt^0-O_v-Ti structure changed from −0.8 |e| to +0.01 |e| during the water dissociation process, indicating the formation of the $Pt^{\delta+}$-OH-Ti structure (Supplementary Fig. S25 and Table S2). This observation aligned with the dynamic evolution of the oxidation state of Pt species at the interface during the reaction.

The participation of hydroxyls in the reaction to generate oxygen vacancies

Generally, the activation and dissociation of H_2O molecule was commonly regarded as the rate-determining step in the WGS reaction, which could be substantiated by H/D kinetic isotope effect (KIE) experiments (Supplementary Fig. S26)[7]. In the association mechanisms of the WGS reaction, surface hydroxyls, formed through H_2O dissociation, served as active intermediates that react with CO to generate products[52]. Therefore, it was crucial to confirm the reactivity of surface hydroxyls constructed on the support of 0.3Pt/(TiO_2-T-500) catalyst during the reaction. As shown in Fig. 3a, CO-TPR measurement after H_2 treatment was conducted to monitor the H_2 generation. Upon CO injection, the H_2 signal for 0.3Pt/(TiO_2-T-500) appeared at 166 °C, which was not only lower than the H_2 formation temperature in the 0.3Pt/(TiO_2-A) catalyst, but also showed the significant increase in the amount of H_2 generated. This results indicated that the surface hydroxyls constructed on the catalyst could be directly consumed by CO to form products. To further elucidate the participation behavior of surface hydroxyls of 0.3Pt/(TiO_2-T-500) in the reaction, mass spectrometry was performed under different conditions with continuous operation (Fig. 3b). Firstly, the WGS reaction condition was implemented to track the consumption of reactants and the formation of products. At 125 °C, the rapid CO consumption occured before the reaction initiation, accompanied by the simultaneous formation of CO_2 and H_2. This phenomenon might originate from the participation of surface hydroxyls on the 0.3Pt/(TiO_2-T-500) catalyst in the reaction, which was further evidenced by the fact that the 0.3Pt/(TiO_2-A) catalyst exhibited no H_2 production before the reaction initiation (Supplementary Fig. S27). Following the WGS reaction, it was observed that there was an absence of H_2 generation after the injection of H_2O, which excluded the presence of the redox pathway[52,53]. After a prolonged high-temperature drying process under Ar atmosphere to remove surface moisture, the temperature programmed surface reaction (TPSR) experiment was conducted. As injecting CO, the distinct signals of CO_2 and H_2 with the ratio of 2:1 were exhibited, which indicated the association mechanism of the catalyst following H_2O dissociation forming hydroxyls as active intermediates (Supplementary Fig. S28a). The similar reaction mechanism was also followed by 0.3Pt/(TiO_2-A) catalyst (Supplementary Fig. S28b). This further demonstrated the

https://doi.org/10.1038/s41467-026-69612-9

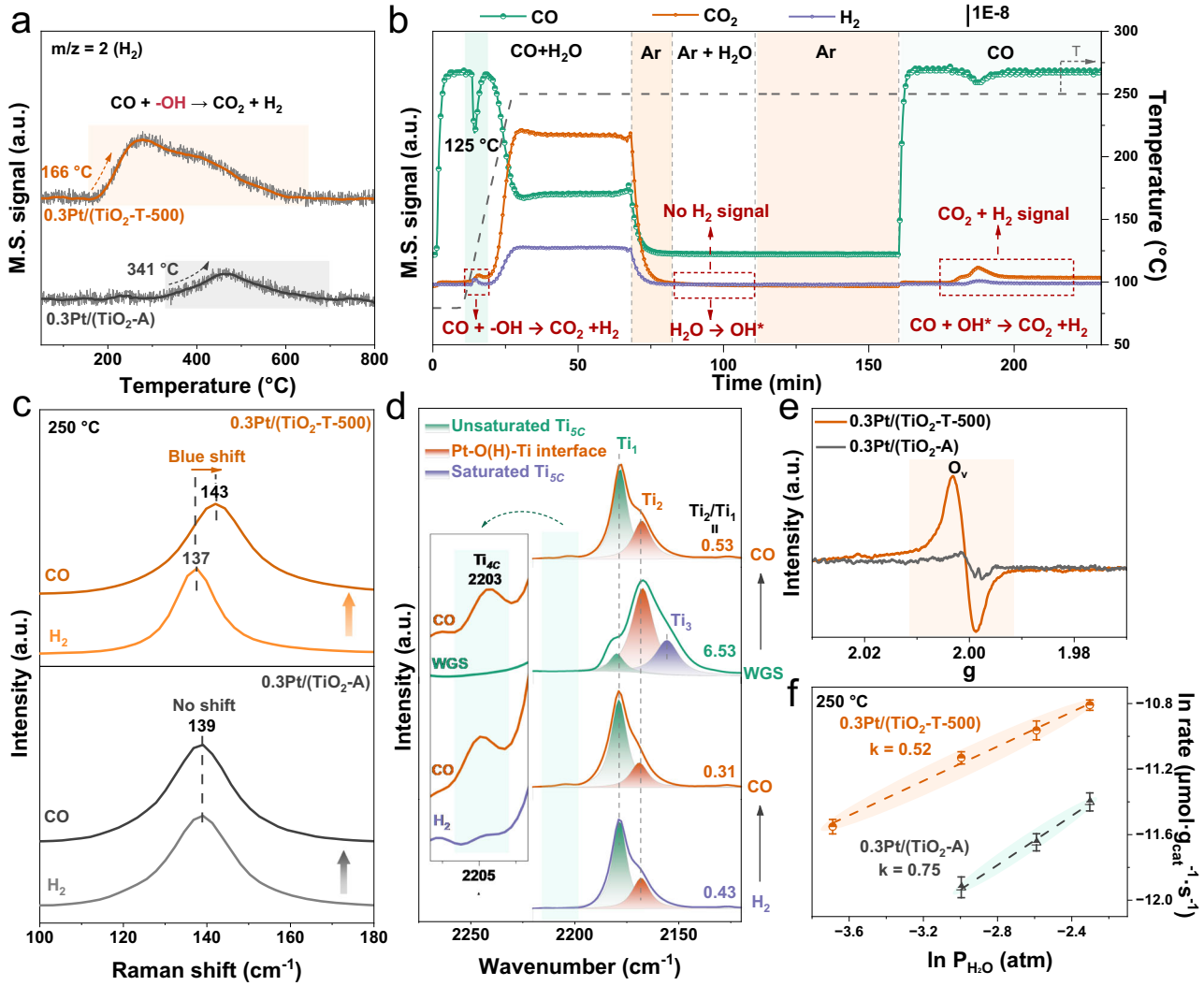

Fig. 3 | Surface hydroxyls consumed by CO to facilitate oxygen vacancy formation for enhanced H_2O dissociation. a CO-TPR profiles of 0.3Pt/(TiO_2-T-500) and 0.3Pt/(TiO_2-A) samples after H_2 treatment. **b** In situ WGS reaction, H_2O dissociation and CO-TPSR of the 0.3Pt/(TiO_2-T-500) catalyst. **c** In situ Raman of 0.3Pt/(TiO_2-A) and 0.3Pt/(TiO_2-T-500) during the switch from H_2 to CO at 250 °C. **d** In situ infrared spectra of 0.3Pt/(TiO_2-T-500) catalyst recorded after various pretreatment conditions at −130 °C. **e** EPR measurement of 0.3Pt/(TiO_2-T-500) and 0.3Pt/(TiO_2-A) after WGS reaction. **f** H_2O kinetic orders of 0.3Pt/(TiO_2-T-500) and 0.3Pt/(TiO_2-A) at 250 °C. The error bars are defined as standard deviation, and the center of each error bar represents the mean value of three independent experiments.

crucial role of surface hydroxyls in the efficient progress of WGS reactions.

Given that the consumption of surface hydroxyls constructed on the catalyst by CO occurred prior to the onset of the reaction, it is imperative to reveal the role of the consumption in surface structure of the catalysts. Firstly, in situ Raman spectroscopy was conducted (Fig. 3c). Upon switching from H_2 to CO, the F_{2g} peak of the 0.3Pt/(TiO_2-T-500) catalyst exhibited the blue shift of 7 cm^{-1}, while that in the 0.3Pt/(TiO_2-A) catalyst remained unchanged[54,55]. A plausible explanation for this difference was that the reaction between CO and the surface hydroxyls of the 0.3Pt/(TiO_2-T-500) catalyst not only generated the products but also facilitated the creation of oxygen vacancies. In addition, in situ infrared spectroscopy at low temperature (−130 °C) was employed by detecting Ti sites after treatment under various conditions at 300 °C (Fig. 3d). The two peaks located at 2179 cm^{-1} and 2164 cm^{-1} appeared after H_2 pretreatment, which were attributed to unsaturated Ti_{5C} sites (denoted as Ti_1) and Pt-O(H)-Ti interfacial sites (denoted as Ti_2), respectively[56,57]. The ratio of the peak areas of Ti_2 to Ti_1 sites (Ti_2/Ti_1) was used to qualitatively represent the content of hydroxyls. Subsequently, the catalyst was further treated with CO at 300 °C and then cooled down to −130 °C for testing. It was found that the Ti_2/Ti_1 ratio decreased from 0.43 to 0.31, indicating that CO consumed the surface hydroxyls. Simultaneously, the peak intensity at 2203 cm^{-1}, attributed to Ti_{4C} sites, increased significantly, which indicated the increase in oxygen vacancies on the TiO_2 surface[56,57]. The above results provided insight into the correlation between the consumption of surface hydroxyl groups by CO and the facilitated formation of oxygen vacancies. After the WGS reaction, the signal of Pt-O(H)-Ti interfacial sites re-emerged abundantly, which was likely attributable to the surface hydroxyls formed via H_2O dissociation during the reaction. Consistent with this, the post-reaction O 1*s* XPS spectra and ATR-IR measurements likewise showed enhanced signals associated with hydroxyl species (Supplementary Fig. S29). Moreover, the weakening signal of the Ti_{4C} and unsaturated Ti_{5C} sites, along with the formation of new saturated Ti_{5C} sites (denoted as Ti_3)[56,57], indicated that oxygen vacancies might be replenished by hydroxyls generated from water dissociation. Afterward, the post-reaction catalyst was also treated with CO. The Pt-O(H)-Ti interfacial sites peak weakened and the Ti_{4C} and unsaturated Ti_{5C} sites peaks increased, which was attributed to the consumption of hydroxyl groups by CO and the concomitant

formation of oxygen vacancies. A reasonable model to explain these observations was that the consumption of hydroxyl groups by CO, whether initially present or formed during the WGS reaction, suggested a link to the formation of oxygen vacancies. Furthermore, the EPR results manifested that the 0.3Pt/(TiO_2-T-500) catalyst did not exhibit significant defects after H_2 pretreatment (Supplementary Fig. S30), while the substantial number of defects emerged following the WGS reaction (Fig. 3e). And the quantity of these defects was significantly higher compared to the 0.3Pt/(TiO_2-A) catalyst. Given the similar size of the Pt species in both catalysts, the variation in oxygen vacancy concentration could be rationalized by the differing levels of surface hydroxylation, which was consistent with the observed correlation between hydroxyl consumption and defect formation.

Furthermore, insights were gained into the behavior of water dissociation on the surface of the 0.3Pt/(TiO_2-T-500) catalyst using isotopic experiments. The catalyst was first subjected to CO-TPR aimed at removing hydroxyl groups. Subsequently, $H_2{}^{18}O$ was introduced for 20 min. Upon switching back to the CO flow, signals for $C^{16}O^{18}O$ were detected by both in situ DRIFTS and mass spectrometry (Supplementary Fig. S31 and S32). This observation suggested the possibility that H_2O dissociated on the catalyst surface. Moreover, 0.3Pt/(TiO_2-T-500) with more defects exhibited the greater capacity for H_2O dissociation, as evidenced by the fact that the reaction order of H_2O at both 250 °C and 290 °C was lower than that of 0.3Pt/(TiO_2-A) catalyst (Fig. 3f and Supplementary Fig. S33). However, the present experiments unfortunately could not confirm the exact active site for H_2O dissociation. Moreover, given the dynamic nature of hydroxyl groups under reaction conditions, their precise role could not be unambiguously assigned to individual steps. Taken together, a plausible framework could be inferred by integrating all available data, namely, that the hydroxyl-tuning strategy resulted in an optimal catalyst concurrently exhibiting higher oxygen vacancy signatures and the greater capacity for water activation.

The enhanced WGS reaction performance by the construction of hydroxyls

The comprehensive optimization of both the electronic structure of the active metal and the surface structure of the support oxide by surface hydroxyl groups has been clearly revealed through the above results, which was summarized in the schematic diagram in Fig. 4a. On one hand, surface hydroxyls facilitated the reduction of the catalyst, thereby forming Pt^0 species that enhanced the adsorption and activation of CO molecules. On the other hand, surface hydroxyls were directly consumed by CO during the reaction, which promoted the formation of oxygen vacancies that enhanced the dissociation of H_2O molecules. Therefore, in contrast to the singular focus on optimizing the state of Pt species or the TiO_2 surface structure reported in the literature, surface hydroxyls specifically achieved the simultaneous enhancement in the activation capability for both reactant molecules in the WGS reaction, thereby working in combination to maximize the catalytic performance.

The WGS reaction was evaluated under the product free gas (2% CO/10% H_2O/N_2). The catalytic activity of 0.3Pt/(TiO_2-T-500) catalyst was significantly higher than that of 0.3Pt/(TiO_2-A) catalyst, whose CO_2 conversion approached nearly 100% at 250 °C (Fig. 4b). The combined evidence from ICP-MS quantification, XPS analysis, and thorough support washing ruled out the contribution of residual Na and Cl from synthesis to the observed activity enhancement (Supplementary Fig. S34 and Table S3). The similar enhanced the performance was also exhibited by catalysts with Pt loadings of 0.1 wt.% and 0.5 wt.% (Supplementary Fig. S35). Moreover, the WGS reaction activity was improved with increasing Pt loading from 0.1 wt.% to 0.3 wt.% on TiO_2-T-500, while further increase of Pt loading to 0.5 wt.% led to inferior activity, which might be caused by saturation of the Pt active site (Supplementary Fig. S36). Thus, 0.3Pt/(TiO_2-T-500) sample turned out as the ideal catalyst, which established the apparent advantage of reaction rate at 225 °C and 250 °C compared to other catalyst systems in the literature (Fig. 4c and Supplementary Table 4). In particular, the catalytic activity of 0.3Pt/(TiO_2-T-500) catalyst reached 1.7×10^4 $\mu mol_{CO} \cdot g_{Pt}^{-1} \cdot s^{-1}$ at 250 °C, which was more than twice that of the previously reported Pt/TiO_2 catalysts. Moreover, the 0.3Pt/(TiO_2-T-500) catalyst exhibited the TOF nearly twofold higher than that of the reference 0.3Pt/(TiO_2-A) catalyst and advantages over other Pt-based catalysts reported in the literature (Supplementary Table 5). It should be noted that these value were derived via normalization using the uncertain dispersion estimate, which was subject to the inherent assumptions (1:1 CO:Pt stoichiometry) and potential interference. Assuming that the CO chemisorption measurements were comparable for the both catalysts, the observation of a markedly higher TOF indicated a potentially greater intrinsic activity of the active sites on the TiO_2-T-500 support. The apparent activation energies (*E*a) obtained from the Arrhenius plots showed the similar *E*a values of 0.3Pt/(TiO_2-T-500) and 0.3Pt/(TiO_2-A) catalysts (Supplementary Fig. S37), which suggested the two samples followed the identical reaction mechanism, consistent with the results of TPSR experiment. Furthermore, the long-term stability test of 0.3Pt/(TiO_2-T-500) catalysts was examined that there was no deactivation with 70 h, which also possessed remarkable cyclic stability during the rising and cooling between 250 °C and 300 °C (Fig. 4d). Correspondingly, Pt 4*f* XPS spectra indicated the slight further reduction of the Pt species during the long-time reaction (Supplementary Fig. S38). In contrast, the 0.3Pt/(TiO_2-A) catalyst exhibited the gradual increase in activity as the reaction progressed, eventually stabilizing after 20 h, although its final activity remained lower than that of the 0.3Pt/(TiO_2-T-500) catalyst. This phenomenon originated from the enhanced electron density of Pt species, as evidenced by the peak shifting to lower binding energy in the post-stability Pt 4*f* XPS characterization (Supplementary Fig. S39). This further confirmed the crucial role of inducing Pt^0 formation for the enhancement of catalytic performance.

Discussion

The comprehensive and targeted modulation of catalytic sites is closely related to the adsorption and activation capability of reactant molecules. In this work, a practical and reproducible hydroxyl-regulation approach via controlled calcination of a titanate precursor was developed to form ~2 nm Pt^0 clusters on the hydroxyl-tuned TiO_2 support. The Pt^0 acted as the active sites enhancing the adsorption and activation for CO molecules. Subsequently, surface hydroxyls also directly participated in the reaction to generate products. Through comprehensive in situ characterizations, it was observed that the consumption of hydroxyls by CO during the reaction was consistent with oxygen vacancy formation. The obtained catalysts with higher oxygen vacancies content exhibited stronger H_2O dissociation capability. The collectively enhanced activation capabilities of both CO and H_2O molecules might be associated with the improved WGS reaction performance. This work has developed a method for controlling the hydroxyl content to optimize catalytic activity, and has provided a reasonable explanation related to multiple characterizations regarding the regulation of hydroxyl on the metal electronic structure and oxide surface structure.

Methods

Preparation of TiO_2 nanotube and subsequent thermal treatment process

The preparation of the TiO_2 tube involved using a hydrothermal technique within Teflon-lined stainless-steel autoclaves[37,58]. In a standard synthesis procedure for the support, 28 g of NaOH (sourced from Sinopharm) was dissolved in 70 mL of deionized water, resulting in a 10 mol/L solution. Subsequently, 2 g of commercial anatase TiO_2 (obtained from Macklin, with the particle size of 25 nm, referred to as

https://doi.org/10.1038/s41467-026-69612-9

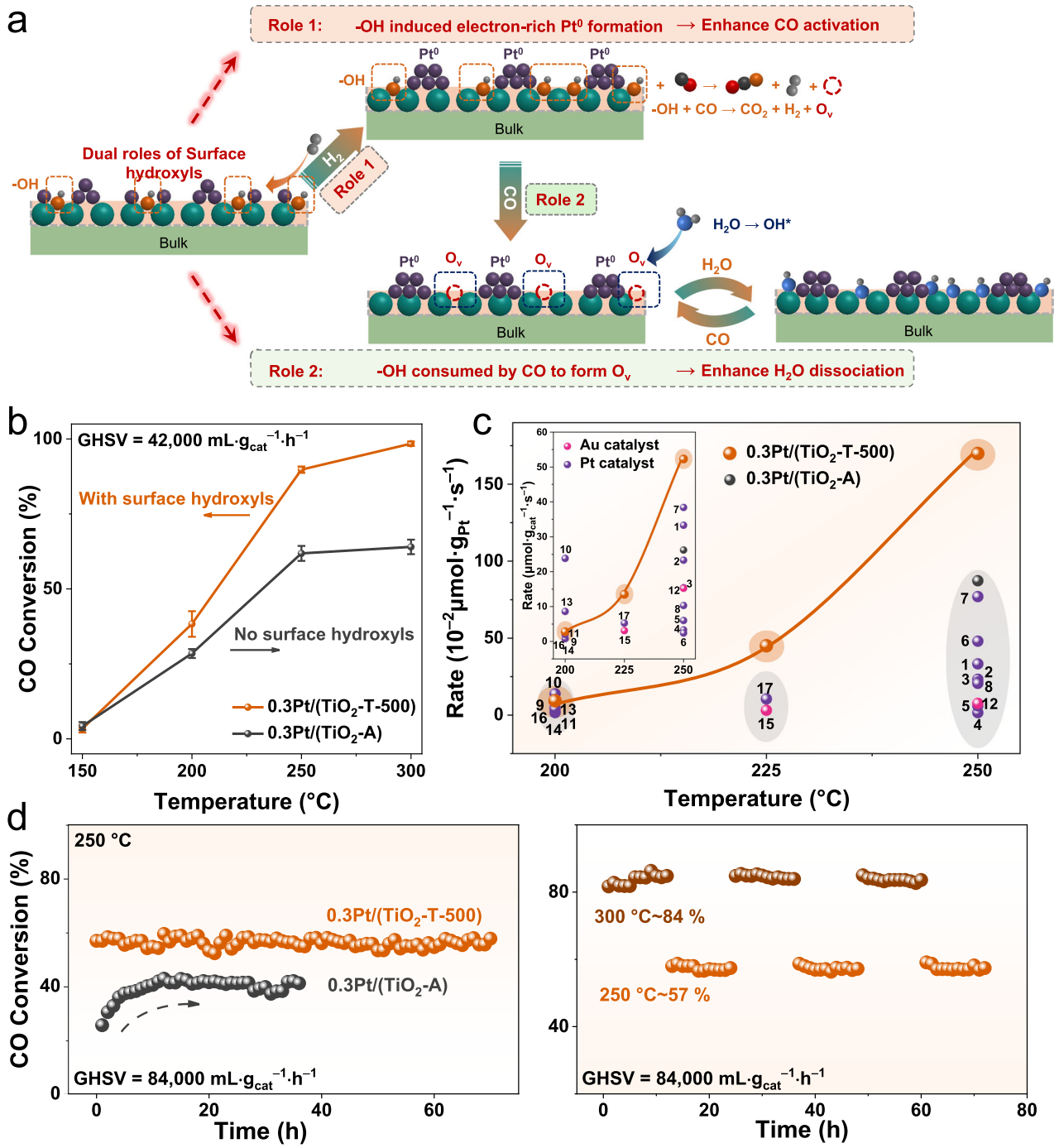

Fig. 4 | Leveraging the roles of surface hydroxyls to enhance reaction performance. a Scheme of dual roles of surface hydroxyls in optimizing the catalyst structure and participating in the reaction. **b** Temperature-dependent CO conversion of 0.3Pt/(TiO_2-T-500) and 0.3Pt/(TiO_2-A) catalysts with 0.3% loading for the WGS reaction. Reaction condition: 2% CO/10% H_2O/N_2, GHSV = 42,000 mL·g_{cat}^{-1}·h^{-1}. **c** Comparison of reaction rate with other Pt/TiO_2 catalysts. **d** The stability 0.3Pt/(TiO_2-T-500) and 0.3Pt/(TiO_2-A) catalysts. Left: long-term stability at 250 °C of 0.3Pt/(TiO_2-T-500) and 0.3Pt/(TiO_2-A) catalysts. Right: the cyclic stability at 300 °C and 250 °C for 0.3Pt/(TiO_2-T-500) at 84,000 mL·g_{cat}^{-1}·h^{-1}.

TiO_2-A) was introduced into the solution and stirred for 1 h at room temperature. Following this, the mixture was subjected to heating at 130 °C for a duration of 24 h. Post-hydrothermal synthesis, the freshly formed precipitates were isolated by filtration and then washed using deionized water and 2 L of a 0.2 M HCl (Sinopharm) aqueous solution, followed by another round of washing with deionized water. The resultant material was then dried in air at 120 °C for 18 h and subsequently ground using a mortar. From this point forward, the TiO_2 tube was designated as TiO_2-T-UC. Subsequently, the TiO_2-T-UC powder was heated in a tube furnace at a rate of 2 °C/min to 200 °C, 400 °C, 500 °C, 600 °C and 800 °C, respectively, and maintained at each temperature for 8 h. The resulting samples were denoted as TiO_2-T-t (t = 200, 400, 500, 600, 800), respectively. The TiO_2-T-wash-500 catalyst was prepared following an identical procedure to that of TiO_2-T-500, with the modification that after washing with 2 L of HCl, the solid was further washed with 5 L of high-purity water. The reference

commercial anatase was also heated in a tube furnace at a rate of 2 °C/min to 500 °C for 8 hours before use.

Preparation of various Pt/TiO_2 catalysts

The platinum−titanium catalysts were prepared according to the wet impregnation (IM) method. First, 0.2 g of TiO_2 powers was added to 20 mL high purity water and dispersed uniformly under vigorous stirring. After stirring the mixture for 30 min, a designed amount of chloroplatinic acid (H_2PtCl_6) solution (0.19 mol/L) was added into the above slurry. The mixture was heated to 90 °C in an oil bath with continuous stirring to facilitate drying. The obtained catalysts were labeled as xPt/(TiO_2-A), xPt/(TiO_2-T-UC) and xPt/(TiO_2-T-t). The symbol x denotes the weight percentage of metallic Pt on the support, which are 0.1, 0.3, and 0.5 wt%.

Inductively coupled plasma mass spectrometry (ICP-MS)

ICP-MS analysis was performed using the NexION 1000 G instrument. The solid catalysts were completely digested using the high-concentration hydrofluoric acid (HF). Approximately 4 mg of the solid catalyst powder was completely digested in 2 mL of HF and subsequently diluted to a final volume of 100 mL. A 10 mL aliquot of this solution was then transferred to a new volumetric flask and diluted again to 100 mL. The resulting solution was used for ICP-MS analysis. The instrument detection limit for the ICP-MS was 50 ppt. By converting this value relative to the initial mass of the catalyst, the corresponding detection limit for elemental content in the solid catalyst is 0.00125 wt.%.

Temperature-programmed reduction with H_2 (H_2-TPR)

H_2-TPR experiments were performed using a Builder PCSA-1000 instrument. Prior to the test, the catalysts (30 mg, 20 − 40 mesh) were pretreated under Ar at 120 °C for 30 min, followed by switching to 5% H_2/Ar. After the baseline was stabilized in hydrogen, the temperature was increased from room temperature to 500 °C at a rate of 10 °C·min^{-1}.

Temperature programmed reduction with CO (CO-TPR)

All these experiments were performed on a lab-made reactor. The catalyst was first pretreated in a 5% H_2/Ar atmosphere for 30 min, then cooled to room temperature, followed by purging with the Ar atmosphere. Subsequently, the atmosphere was switched to 2% CO/Ar, and the temperature was ramped up to 800 °C at a rate of 2 °C/min while simultaneously collecting data.

In situ diffuse reflectance infrared Fourier transform spectroscopy (in situ DRIFTS)

In situ DRIFTS experiments was conducted using a Bruker Vertex 70 FTIR spectrometer equipped with a mercury-cadmium-telluride (MCT) detector. The sample cell (Harrick) featured CaF_2 windows and a heating cartridge. To enable rapid gas switching without dead volume, an electronically controlled quick-switching system was employed. About 20 mg of the sample was filled into the reaction cell and underwent pretreatment in a 5% H_2/Ar atmosphere before any tests were conducted. The spectra were recorded with an integration time of 30 s and a resolution of 4 cm^{-1}, while the background was taken in pure N_2. For the CO adsorption experiment, after the H_2 pretreatment, the 2% CO/He gas was introduced into the reaction cell at 25 °C. Subsequently, the temperature was raised to 250 °C, and the 2% CO/10% H_2O/Ar gas mixture was introduced into the system. After the WGS reaction, the temperature was lowered to room temperature, and 2% CO/He gas was reintroduced. For the CO adsorption−desorption experiments at 250 °C, the catalyst was exposed to 2% CO/He for 10 min, after which it was purged with N_2 and a mixture of N_2 and H_2O, respectively. Upon reaching a new temperature, a fresh background measurement was taken in pure N_2.

In-situ infrared spectroscopy in the transmission mode

In-situ infrared spectroscopy was carried out in a UHV apparatus by an FTIR spectrometer Bruker Vertex 70 (v) with a multichambered ultrahigh vacuum system. The catalyst underwent four different pretreatment methods. Firstly, the sample was pretreated with H_2 in the sample cell at 300 °C and dropped to −130 °C directly. Secondly, the sample was pretreated in the sample cell with H_2 at 300 °C, followed by the switch to CO atmosphere for further treatment, and then cooled down to −130 °C. Thirdly, the sample underwent the WGS reaction treatment in the reactor, then it was transferred to the sample cell and directly cooled down to −130 °C. Lastly, the sample underwent the WGS reaction treatment in the reactor, then it was transferred to the sample cell and further treated with CO at 300 °C, followed by cooling down to −130°C. After the completion of the aforementioned pretreatments and cooling down to −130 °C, adsorption was performed by passing 1×10^{-1} mbar CO accompanied by data collection.

X-ray photoelectron spectroscopy (XPS)

The XPS measurements were carried out on a Thermo Scientific ESCALAB Xi+ XPS spectrometer (Thermo Fisher) with Al Kα radiation (15 kV, 20 mA). Each spectrum was energy-calibrated using the C 1*s* signal at 284.8 eV as a reference.

Raman test

All the ex situ and in situ Raman spectra were acquired by using a Raman microscope system (HORIBA JY) with laser excitation at 473 nm. In the in-situ Raman experiment, the sample was first pretreated with H_2 at 300 °C for 30 min, during which data was collected. Subsequently, the atmosphere was switched to CO, and after maintaining the CO atmosphere for another 30 minutes, data collection was performed.

Catalytic tests

The WGS reaction of platinum-titanium catalysts was conducted in a fixed-bed reactor. 100 mg of the samples (20 − 40 mesh) was placed inside and pretreated with a 5% H_2/Ar gas mixture (70 mL·min^{-1}) at 300 °C for 30 min. Following this, a mixed gas (2% CO/10% H_2O/Ar) was flowed through to carry out the reaction at a gas hourly space velocity of 42,000 mL·g_{cat}^{-1}·h^{-1}. The outlet gas compositions of CO and CO_2 were analyzed online on a Gasboard 3500 IR spectroscopy (Wuhan Sifang Company, China). The CO conversion was defined by the following formula:

$$X_{CO} = \frac{n_{CO}^{in} - n_{CO}^{out}}{n_{CO}^{in}} \times 100 \quad (1)$$

The reaction rates were evaluated by varying the catalyst mass and the flow rate of the reactant gas under conditions where the CO conversion remained below 15%, which were calculated by the following formula:

$$r = \frac{F \times X_{CO}}{m} \quad (2)$$

where F was the molar flow rate of CO in mol·h^{-1} and m was the mass of Pt in the fixed bed.

The TOF value was defined by the following formula:

$$TOF = \frac{r \times M_{Pt}}{D_{Pt}} \quad (3)$$

where M_{Pt} was the molar weight of Pt and D_{Pt} was the dispersion of Pt calculated from the results of CO chemisorption by assuming that the stoichiometric ratio of adsorbed CO/Pt is 1.

During the stability test, the gas mixture was continuously supplied to the fixed-bed reactor at 250 °C for 70 h. Simultaneously, the conversion data were continuously monitored at gas hourly space velocities of 84,000 $mL \cdot g_{cat}^{-1} \cdot h^{-1}$. Moreover, the conversion data during the 70 h process of supplying gas to a fixed-bed reactor while alternating between 250 °C and 300 °C was also recorded. An ice trap was employed to condense the unreacted water following the reactor tube. The concentrations of CO and CO_2 in the outlet gas were monitored using an infrared gas analyzer (Gasboard-3100, manufactured by Wuhan Sifang Company, China). The apparent activation energy (*Ea*) was determined using the same apparatus as for testing the catalytic performance mentioned earlier. A suitable quantity of Pt-supported catalyst was loaded into the reactor, and the temperature and gas flow rate were adjusted to maintain the CO conversion within the range of 5 to 15%. The outlet gas was then analyzed with an infrared gas analyzer (Gasboard-3100, Wuhan Sifang Company, China).

Data availability

The main data supporting the findings of this study are available within the article and its Supplementary Information. Source data of Fig. 1b–e, 2, 3 and 4b–d are provided with this paper. Data are available from the corresponding author upon request. Source data are provided with this paper.

References

1. Ratnasamy, C. et al. Water gas shift catalysis. *Catal. Rev. Sci. Eng.* **51**, 325–440 (2009).
2. Li, Y. et al. Dynamic structure of active sites in ceria-supported Pt catalysts for the water gas shift reaction. *Nat. Commun.* **12**, 1–9 (2021).
3. Chen, A. et al. Structure of the catalytically active copper–ceria interfacial perimeter. *Nat. Catal.* **2**, 334–341 (2019).
4. An, K. et al. High-temperature catalytic reforming of n-hexane over supported and core-shell Pt nanoparticle catalysts: Role of oxide-metal interface and thermal stability. *Nano Lett.* **14**, 4907–4912 (2014).
5. Kattel, S. et al. CO_2 hydrogenation on Pt, Pt/SiO_2 and Pt/TiO_2: importance of synergy between Pt and oxide support. *J. Catal.* **343**, 115–126 (2016).
6. Bonanni, S. et al. Reaction-induced cluster ripening and initial size-dependent reaction rates for CO oxidation on $Pt_n/TiO_2(110)$-(1×1). *J. Am. Chem. Soc.* **136**, 8702–8707 (2014).
7. Kalamaras, C. M. et al. Kinetic and mechanistic studies of the water-gas shift reaction on Pt/TiO_2 catalyst. *J. Catal.* **264**, 117–129 (2009).
8. Gao, M. et al. Ordered mesopore confined Pt nanoclusters enable unusual self-enhancing catalysis. *ACS Cent. Sci.* **8**, 1633–1645 (2022).
9. Tauster, S. J. et al. Strong interactions in supported-metal catalysts. *Science* **211**, 1121–1125 (1981).
10. Campbell, C. T. Catalyst-support interactions: Electronic perturbations. *Nat. Chem.* **4**, 597–598 (2012).
11. van Deelen, T. W. et al. Control of metal-support interactions in heterogeneous catalysts to enhance activity and selectivity. *Nat. Catal.* **2**, 955–970 (2019).
12. Wendt, S. et al. The role of interstitial sites in the Ti_{3d} defect state in the band gap of titania. *Science* **320**, 1755–1759 (2008).
13. Menetrey, M. et al. Reactivity of a reduced metal oxide surface: Hydrogen, water and carbon monoxide adsorption on oxygen defective rutile $TiO_2(110)$. *Surf. Sci.* **524**, 49–62 (2003).
14. Schaub, R. et al. Oxygen vacancies as active sites for water dissociation on rutile $TiO_2(110)$. *Phys. Rev. Lett.* **87**, 266104–1 (2001).
15. Gokhale, A. A. et al. On the mechanism of low-temperature water gas shift reaction on copper. *J. Am. Chem. Soc.* **130**, 1402–1414 (2008).
16. García-Moncada, N. et al. Reactive surface explored by NAP-XPS: why ionic conductors are promoters for water gas shift reaction. *ACS Catal.* **14**, 14947–14957 (2024).
17. Lai, X. M. et al. Heterostructured ceria-titania-supported platinum catalysts for the water gas shift reaction. *ACS Appl. Mater. Interfaces* **14**, 8575–8586 (2022).
18. Ge, S. et al. Revealing the size effect of ceria nanocube-supported platinum nanoparticles in complete propane oxidation. *ACS Catal.* **14**, 2532–2544 (2024).
19. Bezemer, G. L. et al. Cobalt particle size effects in the Fischer-Tropsch reaction studied with carbon nanofiber supported catalysts. *J. Am. Chem. Soc.* **128**, 3956–3964 (2006).
20. Van Den Berg, R. et al. Support functionalization to retard ostwald ripening in copper methanol synthesis catalysts. *ACS Catal.* **5**, 4439–4448 (2015).
21. Parkinson, G. S. et al. Carbon monoxide-induced adatom sintering in a $Pd\text{-}Fe_3O_4$ model catalyst. *Nat. Mater.* **12**, 724–728 (2013).
22. Gunasooriya, G. T. K. K. et al. Key role of surface hydroxyl groups in C-O activation during Fischer-Tropsch synthesis. *ACS Catal.* **6**, 3660–3664 (2016).
23. Saavedra, J. et al. The critical role of water at the gold-titania interface in catalytic CO oxidation. *Science* **345**, 1599–1602 (2014).
24. Wang, J. et al. Confinement-induced indium oxide nanolayers formed on oxide support for enhanced CO_2 hydrogenation reaction. *J. Am. Chem. Soc.* **146**, 5523–5531 (2024).
25. Wang, C. X. et al. Hydroxylated TiO_2-induced high-density Ni clusters for breaking the activity-selectivity trade-off of CO_2 hydrogenation. *Nat. Commun.* **15**, 8290 (2024).
26. Wang, C. et al. Design strategies for high-performance NH_3-SCO catalysts: identifying and modulating direct anchoring sites for Ag on TiO_2. *Environ. Sci. Technol.* **58**, 15343–15353 (2024).
27. Xie, Y. et al. Unraveling the cause of strong metal-support interaction formation: disparities in metal nanoparticle anchoring mechanisms. *Angew. Chem. Int. Ed.* **64**, e202505820 (2025).
28. Mahdavi-Shakib, A. et al. The role of surface hydroxyls in the entropy-driven adsorption and spillover of H_2 on Au/TiO_2 catalysts. *Nat. Catal.* **6**, 710–719 (2023).
29. Xu, S. L. et al. Electrocatalytic hydrogenation boosted by surface hydroxyls-modulated hydrogen migration over nonreducible oxides. *Adv. Mater.* **37**, 2500371 (2025).
30. Baik, Y. et al. Electron and proton storage on separate Ru and BaO domains mediated by conductive low-work-function carbon to accelerate ammonia synthesis. *Nat. Catal.* **8**, 248–256 (2025).
31. Baik, Y. et al. Splitting of hydrogen atoms into proton-electron pairs at BaO-Ru interfaces for promoting ammonia synthesis under mild conditions. *J. Am. Chem. Soc.* **145**, 11364–11374 (2023).
32. Azzam, K. G. et al. Role of Re in $Pt\text{-}Re/TiO_2$ catalyst for water gas shift reaction: A mechanistic and kinetic study. *Appl. Catal. B Environ.* **80**, 129–140 (2008).
33. Zhang, J. et al. Competitive adsorption: reducing the poisoning effect of adsorbed hydroxyl on Ru single-atom site with SnO_2 for efficient hydrogen evolution. *Angew. Chem. Int. Ed.* **61**, e202209486 (2022).
34. Li, Z. et al. Atomic-level design and understanding of hydroxyl-mediated Ag sites with catalytic versatility. *J. Am. Chem. Soc.* **147**, 30326–30338 (2025).
35. Fan, Y. et al. Surface hydroxyl-determined migration and anchoring of silver on alumina in oxidative redispersion. *ACS Catal.* **13**, 2277–2285 (2023).
36. Chang, H. et al. Unlocking methanol synthesis from CO_2 and H_2 on ZnO/ZrO_2 catalysts: surface hydroxyl-mediated activation. *ACS Catal.* **15**, 6005–6017 (2025).
37. Tsai, C. C. et al. Structural features of nanotubes synthesized from NaOH treatment on TiO_2 with different post-treatments. *Chem. Mater.* **18**, 367–373 (2006).

38. Wang, L. et al. Cell responses on a $H_2Ti_3O_7$ nanowire film. *RSC Adv.* **7**, 33606–33613 (2017).
39. Wang, H. et al. Construction of $Pt^{\delta+}$-O(H)-Ti^{3+} species for efficient catalytic production of hydrogen. *ACS Catal.* **13**, 10500–10510 (2023).
40. Lei, H. et al. Thermally triggered redox flexibility of Pt/CeO_2 cluster catalyst against in-situ atomic redispersion. *Angew. Chem. Int. Ed.* **64**, e202509239 (2025).
41. Tang, N. et al. Pt atom-substituted MoC single-atom catalyst for enhancing H_2 production. *ACS Catal.* **14**, 14297–14307 (2024).
42. Liu, H. X. et al. Pt_n–O_v synergistic sites on MoO_x/γ-Mo_2N heterostructure for low-temperature reverse water–gas shift reaction. *Nat. Commun.* **13**, 5800 (2022).
43. Li, K. et al. Carbon deposition on heterogeneous Pt catalysts promotes the selective hydrogenation of halogenated nitroaromatics. *ACS Appl. Mater. Interfaces* **13**, 52193–52201 (2021).
44. Rossi, G. et al. L-edge x-ray absorption resonances in palladium silicides and palladium metal. *Phy. Rev. B* **27**, 5154–5157 (1983).
45. Ding, K. et al. Identification of active sites in CO oxidation and water-gas shift over supported Pt catalysts. *Science* **350**, 189–192 (2015).
46. Dessal, C. et al. Dynamics of single Pt atoms on alumina during CO oxidation monitored by operando X-ray and infrared spectroscopies. *ACS Catal.* **9**, 5752–5759 (2019).
47. Zhou, Y. et al. Interplay of Pt and crystal facets of TiO_2: CO oxidation activity and operando XAS/DRIFTS studies. *ACS Catal.* **6**, 7799–7809 (2016).
48. Resasco, J. et al. Uniformity is key in defining structure-function relationships for atomically dispersed metal catalysts: The case of Pt/CeO_2. *J. Am. Chem. Soc.* **142**, 169–184 (2020).
49. Qiao, B. et al. Single-atom catalysis of CO oxidation using Pt_1/FeO_x. *Nat. Chem.* **3**, 634–641 (2011).
50. Zhang, R. et al. Promoting the cleavage of C–O bonds at the interface between a metal oxide cluster and a CO(0001) support. *ACS Catal.* **10**, 14722–14731 (2020).
51. Fu, Q. et al. Active nonmetallic Au and Pt species on ceria-based water-gas shift catalysts. *Science* **301**, 935–938 (2003).
52. Yu, W. Z. et al. Very high loading oxidized copper supported on ceria to catalyze the water-gas shift reaction. *J. Catal.* **402**, 83–93 (2021).
53. Xu, M. et al. Insights into interfacial synergistic catalysis over Ni@TiO_{2-x} catalyst toward water-gas shift reaction. *J. Am. Chem. Soc.* **140**, 11241–11251 (2018).
54. Wei, S. et al. Au/TiO_2 catalysts for CO oxidation: effect of gold state to reactivity. *J. Phys. Chem. C.* **122**, 4928–4936 (2018).
55. Belgamwar, R. et al. Defects tune the strong metal-support interactions in copper supported on defected titanium dioxide catalysts for CO_2 reduction. *J. Am. Chem. Soc.* **145**, 8634–8646 (2023).
56. Lee, I. et al. Effect of metal nanoparticle size and titania crystallinity on the performance of Au/TiO_2 catalysts for the promotion of carbon monoxide oxidation at cryogenic temperatures. *J. Chem. Phys.* **151**, 054701 (2019).
57. Ke, W. et al. Direct characterization of interface sites in Au/TiO_2 catalysts prepared using atomic layer deposition. *Chem. Catal.* **4**, 100977 (2024).
58. Pappas, D. K. et al. Novel manganese oxide confined interweaved titania nanotubes for the lowerature selective catalytic reduction (SCR) of NO_x by NH_3. *J. Catal.* **334**, 1–13 (2016).

Acknowledgements

This work was funded by the National Science Fund for Distinguished Young Scholars of China (22225110, C.-J.J.), the National Key Research and Development Program of China (2021YFA1501103, C.-J.J.), the National Science Foundation of China (22271177, W.-W.W. and 22301163, X.-P.F.), the Science Foundation of Shandong Province of China (ZR2023ZD21, C.-J.J.; ZR2023QB109 and 2024HWYQ-006, X.-P.F.). We thank the Center of Structural Characterizations and Property Measurements at Shandong University. We thank the beamline scientists at the European Synchrotron Radiation Facility (ESRF: BM23, CH-7703) and ESRF for the provision of the beamtime.

Author contributions

C.-J. Jia supervised the work; C.-X. Wang, W.-W. Wang and X.-P. Fu designed the experiments; C.-X. Wang analyzed the results and wrote the manuscript; C.-X. Wang and W.-W. Wang performed the in situ DRIFTS, Raman and XPS; and C.-X. Wang performed the catalysts preparation, tests, and characterization; F. R. Wang and H.-X. Liu provided the XAS measurements and data analysis.

Competing interests

The authors declare no competing interests.

Additional information

Supplementary information The online version contains supplementary material available at https://doi.org/10.1038/s41467-026-69612-9.

Correspondence and requests for materials should be addressed to Wei-Wei Wang or Chun-Jiang Jia.

Peer review information *Nature Communications* thanks the anonymous reviewers for their contribution to the peer review of this work. A peer review file is available.

Reprints and permissions information is available at http://www.nature.com/reprints

Publisher's note Springer Nature remains neutral with regard to jurisdictional claims in published maps and institutional affiliations.

Open Access This article is licensed under a Creative Commons Attribution-NonCommercial-NoDerivatives 4.0 International License, which permits any non-commercial use, sharing, distribution and reproduction in any medium or format, as long as you give appropriate credit to the original author(s) and the source, provide a link to the Creative Commons licence, and indicate if you modified the licensed material. You do not have permission under this licence to share adapted material derived from this article or parts of it. The images or other third party material in this article are included in the article's Creative Commons licence, unless indicated otherwise in a credit line to the material. If material is not included in the article's Creative Commons licence and your intended use is not permitted by statutory regulation or exceeds the permitted use, you will need to obtain permission directly from the copyright holder. To view a copy of this licence, visit http://creativecommons.org/licenses/by-nc-nd/4.0/.

© The Author(s) 2026